Nanoscale Advances

ROYAL SOCIETY OF CHEMISTRY

COMMUNICATION

View Article Online
View Journal | View Issue

Cite this: *Nanoscale Adv.*, 2025, **7**, 4559

Received 30th April 2025
Accepted 15th June 2025

DOI: 10.1039/d5na00423c

rsc.li/nanoscale-advances

Engineering BSA-CAT-Ir nanoparticles for enhanced sonodynamic therapy *via* alleviating tumor hypoxia†

Qiufang Gong,‡[a] Lixuan Huo,‡[a] Shiyi Xiong,[a] Yingying Han,[a] Xuefen Zhao,[a] Lutong Wen,[a] Jiaxi Ru,[a] Hongyu Zhang,[a] Fang Yang,*[a] Guosheng Song*[b] and Chao Liang*[a]

Sonodynamic therapy (SDT) has received extensive attention in tumor treatment due to its unique advantages. However, the hypoxic tumor microenvironment substantially restricts the sonodynamic effect. In this work, BSA-CAT-Ir nanoparticles were successfully developed to overcome the limitations of SDT in solid hypoxic tumors. The nanoparticles can alleviate tumor hypoxia by catalyzing the decomposition of overexpressed hydrogen peroxide in tumors to generate oxygen, thereby enhancing the efficacy of SDT. *In vitro* and *in vivo* experiments demonstrated that BSA-CAT-Ir nanoparticles significantly inhibited tumor growth under ultrasound, providing an effective strategy for tumor hypoxia modulation and SDT resistance suppression.

Sonodynamic therapy (SDT), a novel non-invasive cancer treatment, combines low-intensity ultrasound with sonosensitizers.[1,2] In SDT, ultrasound activates the sonosensitizers, causing them to release energy and generate reactive oxygen species (ROS) that are capable of killing tumor cells. Compared with other treatment methods, ultrasound has good tissue penetration and can penetrate deep into human tissues. This gives SDT obvious advantages in the treatment of deep-seated tumors. SDT also has the characteristics of non-invasiveness or minimal invasiveness, with good patient tolerance and relatively small side effects during the treatment process. These advantages make SDT show great application potential in cancer treatment and other disease treatment fields.[3–5] Studies have shown that during sonodynamic treatment, the generation of ROS by sonosensitizers under ultrasound follows the Type II mechanism, that is, the excited-state sonosensitizer directly transfers energy to oxygen molecules, exciting them to singlet oxygen. However, in the hypoxic tumor microenvironment, the oxygen concentration is low, and the probability of energy transfer between the sonosensitizer and oxygen molecules is reduced, resulting in a decrease in the generation of singlet oxygen and thus weakening the killing effect on tumor cells. On the other hand, sonodynamic treatment itself also consumes oxygen, further aggravating the hypoxia degree of tumors.[6–8]

Due to abnormal angiogenesis and insufficient blood supply, hypoxia is an important environmental feature of advanced solid tumors. It not only promotes the proliferation and metastasis of tumor cells but is also one of the main obstacles in the tumor treatment process. Therefore, regulating the hypoxic state at the tumor site is considered as an effective strategy to improve the treatment effect of cancer, especially for treatments that require oxygen participation.[9,10] To improve the treatment effect, hyperbaric oxygen therapy is currently mainly used clinically. Patients receive radiotherapy in a hyperbaric oxygen chamber to inject more oxygen into the tumor. However, due to the lack of tumor-specific oxygen delivery, hyperbaric oxygen therapy also brings serious adverse reactions such as barotrauma.[11,12] In recent years, nano biomaterials such as fluorides and metal–organic frameworks have been developed as carriers to deliver oxygen to tumor tissues to alleviate the hypoxia.[13–16] However, the oxygen loading/release efficiency of the nano-oxygen-supply system is still low. Developing an efficient and safe strategy to improve tumor hypoxia is of great significance for improving the efficacy of sonodynamic therapy.

Another major factor restricting the efficacy of sonodynamic therapy is the nature of the sonosensitizer. Currently, most sonosensitizers used for SDT are based on organic dyes, including phthalocyanines, porphyrins and their derivatives.[17–19] However, the reported sonosensitizers usually have a relatively low molar extinction coefficient, resulting in the need for high doses. In addition, in the physiological environment, they are easily affected by factors such as pH value and enzymes, and degradation or structural changes occur, affecting the sonodynamic treatment effect. Iridium(III) complexes have

[a]*Institute for Advanced Research, Affiliated Cixi Hospital of Wenzhou Medical University, Ningbo 315300, P. R. China. E-mail: St_hyz@126.com; liangchao@wmu.edu.cn*

[b]*State Key Laboratory for Chemo/Bio-Sensing and Chemometrics, College of Chemistry and Chemical Engineering, Hunan University, Changsha 410082, P. R. China. E-mail: songgs@hnu.edu.cn*

† Electronic supplementary information (ESI) available. See DOI: https://doi.org/10.1039/d5na00423c

‡ Qiufang Gong and Lixuan Huo contributed equally to this work.

received extensive attention as photosensitizers and sonosensitizers due to their ideal photophysical properties, large Stokes shift, and high intersystem crossing ability.[20–23] However, the poor water-solubility of iridium(III) complexes limits their biomedical applications.

Catalase, as a biological enzyme, usually has extremely high catalytic efficiency and can significantly accelerate the rate of chemical reactions under mild conditions, and its catalytic efficiency is higher than that of other materials. In addition, catalase has a high degree of specificity for substrates, and can accurately catalyze specific reactions, reducing the occurrence of side reactions. Catalase is a naturally occurring substance in living organisms, has good compatibility with the tissues and cells of organisms, and generally does not cause immune reactions or other adverse reactions when applied in organisms.

In this work, we cross-linked bovine serum albumin (BSA) and catalase (CAT) to obtain a biocompatible nanocomplex as an efficient carrier for iridium(III) complexes (Ir429), thereby developing BSA-CAT-Ir nanoparticles with good stability (Scheme 1 & Fig. S1†). After tail-vein injection, the nanoparticles can be highly enriched at the tumor site. CAT catalyzes the overexpressed hydrogen peroxide in the tumor to rapidly generate oxygen. *In vitro* immunofluorescence results show that BSA-CAT-Ir can effectively alleviate the hypoxic tumor microenvironment. Under ultrasound, compared with the control group, tumor growth in the BSA-CAT-Ir treatment group was significantly inhibited. The BSA-CAT-Ir nanoparticles with good stability developed in this work can effectively improve the sonodynamic therapy efficacy of iridium(III) complexes through the regulation of the hypoxic microenvironment.

The nanocomplex was obtained by cross-linking BSA and CAT using glutaraldehyde. The average size of the prepared BSA-CAT nanocomplex was measured to be about 120 nm by dynamic light scattering (DLS), which was significantly larger than the average size of free BSA and CAT, indicating the successful cross-linking of BSA and CAT (Fig. 1a). Observed by transmission electron microscopy (TEM), the obtained BSA-CAT nanocomplex showed a uniformly distributed spherical morphology with an average size of about 110 nm, similar to that measured by DLS (Fig. 1b). Through hydrophobic interaction, the Ir complex (Ir429) was loaded onto the BSA-CAT

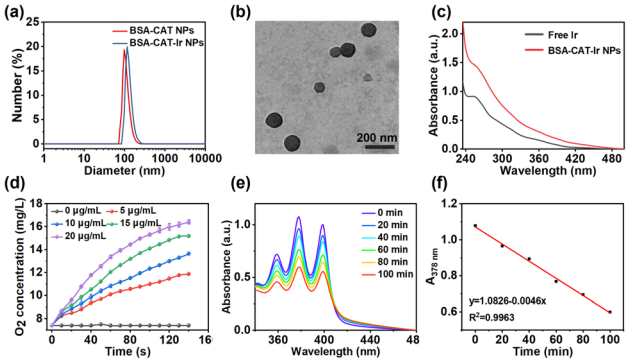

Fig. 1 Characterization of BSA-CAT-Ir NPs. (a) Hydrodynamic diameters of BSA NPs and BSA-CAT-Ir NPs measured by DLS. (b) TEM image of BSA-CAT NPs. (c) UV-vis-NIR absorption spectra of free Ir, and BSA-CAT-Ir NPs. (d) Oxygen production efficacy of BSA-CAT NPs in the H_2O_2 aqueous solution at different concentrations of CAT. (e) Time-dependent oxidation of ABDA indicating $^1O_2$ generation by BSA-CAT-Ir NPs under US irradiation (0.3 W cm^{-2}, 3 MHz). (f) Rate constant for ABDA decomposition at 378 nm in the presence of BSA-CAT-Ir NPs under US irradiation (0.3 W cm^{-2}, 3 MHz).

nanocomplex to obtain the BSA-CAT-Ir nanoparticles. By comparing the UV-vis-NIR absorption spectra of BSA-CAT-Ir and free Ir, BSA-CAT-Ir showed obvious characteristic absorption peaks of Ir, indicating the successful loading of Ir (Fig. 1c). To further verify the stability of BSA-CAT-Ir nanoparticles, they were dispersed in different solvents (H_2O, PBS, 1640 medium). The particle size and potential of BSA-CAT-Ir nanoparticles did not change significantly within seven days, indicating that the nanoparticles had good stability (Fig. S2a & b†).

The catalytic activity of CAT in BSA-CAT was measured by the ammonium molybdate method. Compared with free CAT molecules, the catalytic activity in BSA-CAT was retained at about 90% (Fig. S3†). We further detected the performance of CAT in catalyzing the decomposition of hydrogen peroxide (H_2O_2) using a portable oxygen meter. The results showed that BSA-CAT could effectively decompose H_2O_2 to produce oxygen (Fig. 1d). To further verify the performance of the sonosensitizer Ir in generating singlet oxygen under ultrasound, we used ABDA as a singlet oxygen probe. Without US, there were no significant change in the absorbance of ABDA (Fig. S4b & c†). As shown in Fig. 1e & S4a,† with the prolongation of the ultrasound time, the characteristic absorption of ABDA in BSA-Ir and BSA-CAT-Ir gradually decreased, indicating an increase in the content of singlet oxygen. Without ultrasound, the oxidation of ABDA by BSA-CAT-Ir and BSA NPs-Ir was very slight.

The cellular uptake of different nanoparticles was studied by confocal microscopy. 4T1 cells were incubated with BSA-CAT-Ir at the same concentration for different time periods. After co-incubation for 6 hours, obvious fluorescence signals could be observed. As time went on, more nanoparticles were taken up, indicating that 4T1 cells had a good uptake ability for BSA-CAT-Ir (Fig. 2a and b). Based on this, we used 2,7-dichlorofluorescin diacetate (DCFH-DA) to study the generation of intracellular ROS under ultrasound treatment. As shown in Fig. 2c and d, the fluorescence signals of the control group, BSA-CAT-Ir group,

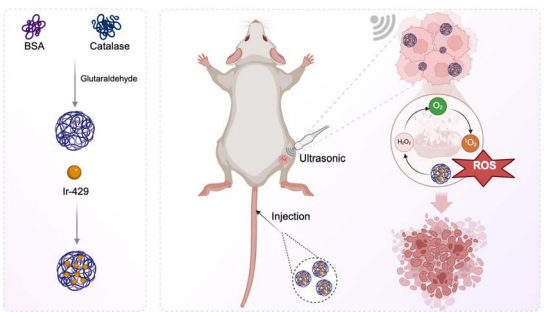

Scheme 1 A scheme illustrating the synthesis process of BSA-CAT-Ir NPs and their performance on enhanced sonodynamic therapy *via* alleviating tumor hypoxia.

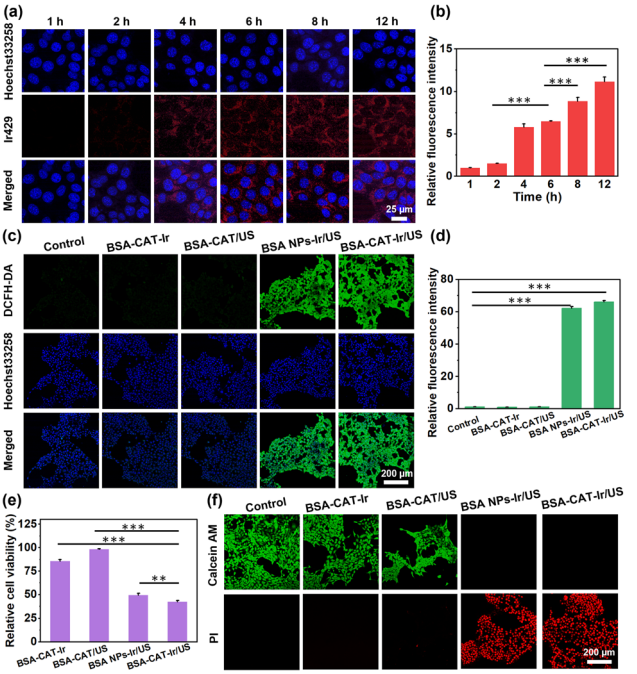

Fig. 2 *In vitro* cell experiments. (a) Confocal fluorescence images of 4T1 cells incubated with BSA-CAT-Ir NPs for different time. (b) Semi-quantitative analysis of fluorescence intensity. (c) Confocal images of 4T1 cells stained with DCFH-DA (green) after various treatments and (d) semi-quantitative analysis of fluorescence intensity. (e) Relative cell viability of 4T1 cells after various treatments. (f) Confocal images of 4T1 cells stained with calcein AM (green, live cells) and propidium iodide (red, dead cells) after different treatments.

and BSA-CAT/US group were weak. In contrast, strong green fluorescence could be observed in the cells of BSA-Ir and BSA-CAT-Ir under the action of US. These results indicated that a large amount of $^1O_2$ was generated in the cells, which could kill cancer cells. The MTT assay was further used to study the *in vitro* sonodynamic treatment effect. When cancer cells incubated with BSA-CAT NPs or BSA-CAT-Ir, the cell viability did not decrease, indicating that BSA-CAT NPs or BSA-CAT-Ir has non toxicity without US (Fig. S5†). After incubating different nanomaterials with 4T1 cells for 4 h (Ir concentration was 20 μM) and then treating them with ultrasound, the results showed that the cell viability was the lowest in the BSA-CAT-Ir/US group, indicating the best treatment effect (Fig. 2e). In addition, to visually display the sonocytotoxicity of BSA-CAT-Ir to 4T1 cells, the treated 4T1 cells were co-stained with calcein AM (AM) and propidium iodide (PI). As expected, only incubation with BSA-CAT-Ir or BSA-CAT NRs under the action of US showed a strong AM signal and a weak PI signal (Fig. 2f). While strong red fluorescence could be observed in BSA-Ir and BSA-CAT-Ir under the action of US. These results proved that Ir had high sonotoxicity to tumor cell.

Before *in vivo* treatment, we firstly studied the biological behavior of BSA-CAT NPs. After labeling BSA-CAT nanoparticles with Cy5.5 fluorescent dye, 200 μL of BSA-CAT NPs was injected *via* the tail vein, and imaging was performed at different times using a small animal *in vivo* imaging system (IVIS Lumia XRMS Series III). As shown, the fluorescence intensity at the tumor site of the mouse increased with time and reached a peak after 8 hours (Fig. 3a). After the imaging was completed, the tumor tissues and various organs of each group were collected for *ex vivo* imaging and semi-quantitative analysis. The results showed that the signal values of the tumor, liver, and kidney were high, further demonstrating the efficient tumor enrichment of the nanoparticles and indicating that the nanoparticles might be mainly excreted through the liver and kidney pathways.

We further studied the antitumor efficacy in a 4T1 tumor-bearing mouse model. The tumor-bearing mice were randomly divided into 5 groups (5 mice in each group): (1) control group; (2) BSA-CAT-Ir; (3) BSA-CAT/US (0.3 W cm^{-2}, 3 MHz, 20 minutes ultrasound treatment); (4) BSA-Ir/US (0.3 W cm^{-2}, 3 MHz, 20 minutes ultrasound treatment); (5) BSA-CAT-Ir/US (0.3 W cm^{-2}, 3 MHz, 20 minutes ultrasound treatment). Thereafter, the tumor was monitored by vernier caliper. As shown in Fig. 3b, compared with the control group, there was no significant difference in

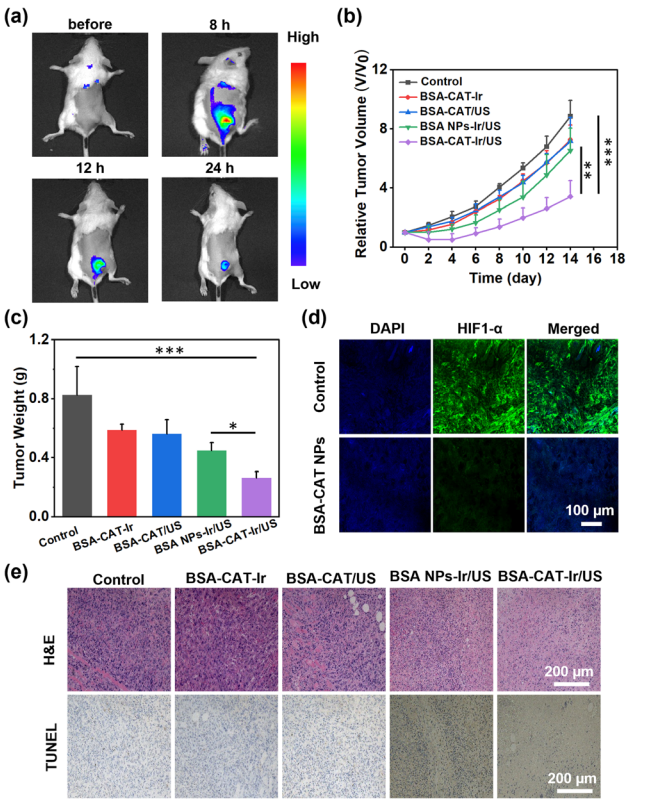

Fig. 3 *In vivo* sonodynamic therapy. (a) *In vivo* fluorescence images of 4T1 tumor-bearing mice were recorded before and 8, 12 and 24 hours after i.v. Cy5.5-BSA-CAT NPs injection. (b) Tumor growth curves of mice after various treatments. Error bars were standard errors (±SD) based on five mice in each group. Statistical significance was calculated with two-tailed Student's *t*-test (***$p < 0.001$, **$p < 0.01$, or *$p < 0.05$). (c) Average tumor weights of mice at 14 days post various treatments as shown in (d). (d) Representative tumor hypoxia immunofluorescence staining of tumor slices collected from the mice treated with PBS(control) and BSA-CAT NRs injections. Blue and green stands for cell nuclei, and positive hypoxic area respectively. (e) Microscopy photos of H&E and TUNEL stained tumor slices. Tumors tissue were collected from mice at 24 h post various treatments. The experiment was repeated three times independently with similar results.

tumor growth in the BSA-CAT-Ir group and the BSA-CAT/US group. The tumor in the BSA-Ir/US group showed a certain inhibitory effect. Notably, the tumor growth inhibition efficiency in the BSA-CAT-Ir/US group was significant. At the end of the experiment, the mice in different groups were sacrificed, and the tumors were collected for weighing (Fig. 3c). The average weight of the tumor in the BSA-CAT-Ir/US group was the smallest, further indicating its good treatment effect. This might be due to the relieve of the hypoxic tumor microenvironment, which effectively increased the production of ROS during sonodynamic treatment. To this end, we verified the improvement of the hypoxic microenvironment inside the tumor through *in vitro* immunofluorescence staining. The results showed that 24 hours after tail-vein injection of BSA-CAT-Ir, the tumor slices showed a significantly reduced positive hypoxia area, indicating obvious alleviation of tumor hypoxia (Fig. 3d & S6†).

In addition, the effects of ultrasound treatment were evaluated by hematoxylin and eosin (H&E) staining and TdT-mediated dUTP nick-end labeling (TUNEL) assays. 24 hours after various treatments, the mice were sacrificed to collect their tumors for histological analysis. Consistent with the above data, we observed severe damage to the tumor tissue in the BSA-CAT-Ir/US group. While in the control group, BSA-CAT-Ir group, and BSA-CAT/US group, no obvious tissue damage was observed (Fig. 3e). On 14th day after the above-mentioned various treatments, the main organs of the mice were collected for H&E stained assays. No obvious tissue damage was found from these sections, indicating that the prepared nanoparticles had good biocompatibility (Fig. S7†).

In summary, to overcome the limitations of SDT in the treatment of solid hypoxic tumors, BSA-CAT-Ir nanoparticles were successfully developed. Catalase was used to catalyze the generation of oxygen from overexpressed hydrogen peroxide inside the tumor, thereby downregulating the expression of hypoxia-inducible factor (HIF-1α). The improvement of the tumor microenvironment mediated by BSA-CAT-Ir can give full play to the advantages of SDT. *In vitro* and *in vivo* experimental results have proved that BSA-CAT-Ir can enhance the efficacy of SDT and significantly inhibit tumor growth under ultrasound. The BSA-CAT-Ir nanoparticles will provide an effective strategy for achieving tumor hypoxia modulation and effectively inhibiting the hypoxia-induced resistance of SDT in tumor treatment.

Data availability

The all data generated in this study are available from the corresponding authors upon reasonable request.

Conflicts of interest

There are no conflicts to declare.

Acknowledgements

This work was supported by Zhejiang Provincial Natural Science Foundation (LQN 25C100009), Ningbo Natural Science Foundation (2023J261, 2023J395).

Notes and references

1 Y. Zhang, X. Zhang, H. Yang, L. Yu, Y. Xu, A. Sharma, P. Yin, X. Li, J. S. Kim and Y. Sun, *Chem. Soc. Rev.*, 2021, **50**, 11227–11248.
2 Y. Yang, J. Huang, M. Liu, Y. Qiu, Q. Chen, T. Zhao, Z. Xiao, Y. Yang, Y. Jiang and Q. Huang, *Adv. Sci.*, 2023, **10**, 2204365.
3 X. Cao, M. Li, Q. Liu, J. Zhao, X. Lu and J. Wang, *Small*, 2023, **19**, 2303195.
4 D. Li, Y. Yang, D. Li, J. Pan, C. Chu and G. Liu, *Small*, 2021, **17**, 2101976.
5 Z. Gong and Z. Dai, *Adv. Sci.*, 2021, **8**, 2002178.
6 Z. Jiang, W. Xiao and Q. Fu, *J. Contr. Release*, 2023, **361**, 547–567.
7 L. Sun, Y. Cao, Z. Lu, P. Ding, Z. Wang, F. Ma, Z. Wang and R. Pei, *Nano Today*, 2022, **43**, 101434.
8 N. Tao, H. Li, L. Deng, S. Zhao, J. Ouyang, M. Wen, W. Chen, K. Zeng, C. Wei and Y.-N. Liu, *ACS Nano*, 2021, **16**, 485–501.
9 T. Hompland, C. S. Fjeldbo and H. Lyng, *Cancers*, 2021, **13**, 499.
10 J. Du, T. Shi, S. Long, P. Chen, W. Sun, J. Fan and X. Peng, *Coord. Chem. Rev.*, 2021, **427**, 213604.
11 Y. Zhang, Y. Zhou, Y. Jia, T. Wang and D. Meng, *Front. Med.*, 2023, **10**, 1160774.
12 A. B. Marcinkowska, N. D. Mankowska, J. Kot and P. J. Winklewski, *Neuropsychol. Rev.*, 2022, 1–28.
13 C. Ruan, K. Su, D. Zhao, A. Lu and C. Zhong, *Front. Chem.*, 2021, **9**, 649158.
14 M.-Z. Zou, W.-L. Liu, H.-S. Chen, X.-F. Bai, F. Gao, J.-J. Ye, H. Cheng and X.-Z. Zhang, *Natl. Sci. Rev.*, 2021, **8**, nwaa160.
15 C.-S. Yuan, Z.-W. Deng, D. Qin, Y.-Z. Mu, X.-G. Chen and Y. Liu, *Acta Biomater.*, 2021, **125**, 1–28.
16 Y. Pan, L. Liu, X. Mou and Y. Cai, *ACS Nano*, 2023, **17**, 20875–20924.
17 L. Sun, P. Wang, J. Zhang, Y. Sun, S. Sun, M. Xu, L. Zhang, S. Wang, X. Liang and L. Cui, *Biomater. Sci.*, 2021, **9**, 1945–1960.
18 M. Tian, Y. Li, Y. Li, T. Yang, H. Chen, J. Guo, Y. Liu and P. Liu, *Small*, 2024, **20**, 2400654.
19 S. Liao, M. Cai, R. Zhu, T. Fu, Y. Du, J. Kong, Y. Zhang, C. Qu, X. Dong and J. Ni, *Mol. Pharm.*, 2023, **20**, 875–885.
20 D. Tang, M. Cui, B. Wang, C. Xu, Z. Cao, J. Guo, H. Xiao and K. Shang, *Adv. Mater.*, 2024, **36**, 2406815.
21 P. Nittayacharn, E. Abenojar, M. La Deda, L. Ricciardi, G. Strangi and A. A. Exner, *Bioconjugate Chem.*, 2021, **33**, 1057–1068.
22 C. Li, Y. Gao, Y. Wang, J. Wang, J. Lin, J. Du, Z. Zhou, X. Liu, S. Yang and H. Yang, *Adv. Funct. Mater.*, 2023, **33**, 2210348.
23 J. Zhu, A. Ouyang, Z. Shen, Z. Pan, S. Banerjee, Q. Zhang, Y. Chen and P. Zhang, *Chin. Chem. Lett.*, 2022, **33**, 1907–1912.